Chapter – 6

Structure-activity relationship for electrocatalysis in rocksalt and spinel based multicomponent oxides and its derivatives

6.1. Introduction

The accelerated depletion of fossil fuel reserves coupled with rapidly changing geo-political scenario has put alternative energy sources, its conversion and storage at the forefront of research activities globally [1-3]. Renewable-energy based economy is driving the modern society away from fossil-fuel based economy slowly and steadily [4-6]. However, the age-old tradition of producing hydrogen using coal or natural gas is still prevalent, continuously degrading the environment in the process and is likely to be ceased as an option in the near future [4,5]. In this context, production, storage and transportation of hydrogen has emerged as the new energy currency [6-8]. However, most renewable sources of energy are intermittent and spurious, which calls for material containers for efficient energy storage and conversion techniques [9,10]. Thus, the ability to split water efficiently and effectively to produce clean hydrogen plays a vital role in energy sciences with the potential to help decarbonize the global energy harvesting system [6-8]. There are three broad ways of splitting water to obtain clean hydrogen i.e. thermochemical, electrochemical and photochemical methods which produces oxygen through oxygen evolution reaction (OER) at the anode and hydrogen through hydrogen evolution reaction (HER) at the cathode as redox pairs [11]. The major bottleneck in electrochemical water-splitting experiments is the high activation barrier for a 4-electron transfer process for efficient OER and HER making it kinetically extremely sluggish, requiring very high input energy as overpotential to break the O-H bonds [12]. Thus, developing efficient electrocatalysts and understanding the properties in relation to its composition, phase(s) and structure promises the way forward [13-15]. Noble metal oxides IrO_2 and RuO_2 remains to be the state-of-the-art electrocatalysts, however, their extremely high cost and scarcity has led to a resurgence of developing multicomponent oxides in the last few decades [15].

Moreover, there is a dearth of literature so far, the structure-property correlation of high entropy oxides or multicomponent oxides (HEOs/MCOs) are concerned. The current work has been carried out to understand the factors affecting the electrocatalytic performances of phase pure rocksalt and spinel HEOs, two-phase mixture of rocksalt and spinel along with multi-phase MCOs. The compositions have been tested against linear sweep voltammetry (LSV), cyclic voltammetry (CV) and obtained Tafel slopes along with overpotential values. The results have been correlated with the experimental findings from SEM, XRD and TEM studies in an attempt to understand the relationship between electrocatalytic activity and phase, microstructure and chemistry.

6.2. Sample preparation and experimental setup

Precursor metal oxides Co(II,III)O, Cr(III)O, Cu(II)O, Fe(II,III)O, MgO, Mn(III)O, NiO and ZnO of high purity (>99.8%) were procured from either Alfa Aesar or Sigma Aldrich. Weighed powder in stoichiometric proportions were taken and mixed thoroughly in a mortar and pestle. Mixed powders of different equimolar compositions i.e. (CoMgNi)-oxide, (CoMgMnNi)-oxide, (CoCaFeMgNi)-oxide, (CoCuMgNiZn)-oxide and (Co(Mg/Cr)FeMnNi)-oxide were green compacted in an uniaxial hydraulic press under 4T load. The green compacted pellets were sintered at either 1323K or 1473K for 10 h followed by water quenching in an air-atmosphere tube furnace. Moreover, sintered pellet from couple of compositions were further subjected to ageing treatment at 723K for 120 h.

Electrocatalytic activity for efficient catalysis in OER experiments were carried out on an Electrochemical workstation (CORRTEST CS 350) using CS Studio. A three-electrode setup has been used with glassy carbon as working electrode, Ag/AgCl as reference electrode, graphite rod as counter electrode and 1M KOH solution as electrolyte. The glassy

carbon electrode was cleaned and polished (mirror finish) using high purity alumina and "ink" of each composition was drop-cast onto the glassy carbon electrode (0.071 cm^2 surface area). For preparing the ink, thin slices were cut from the sintered pellets of various compositions and it was ground into powder by mortar and pestle after which 1 mg of the specimen powder was mixed with 10 μL of 5wt% Nafion solution and 350 μL of ethanol in a vial. The vial was then ultrasonicated for sufficient time before ~ 7 μL of the ink was pipetted out on to the glassy carbon electrode. After the setup was complete, linear sweep voltammetry (LSV), cyclic voltammetry (CV) and electron impedance spectroscopy (EIS) was carried out multiple times on each of the compositions for reproducibility of results. For phase and microstructural characterization, standard metallographic procedure was carried out before its examination by XRD, SEM and TEM as mentioned in chapters 3, 4 and 5. Finally, an attempt has been made to correlate the electrocatalytic activity of the multicomponent oxides in relation to its phase, crystal structure, microstructure and chemistry.

6.3. Results and Discussion

All the sintered, quenched, aged equimolar multicomponent oxides (MCOs) and high entropy oxides (HEOs) were tested for linear sweep voltammetry (LSV) response at a scan rate of 10 mV/sec under alkaline condition. The current density (J) vs reduced hydrogen potential (RHE) plots of sintered and quenched (CaCoFeMgNi)-oxide, (CoFeMgMnNi)-oxide, (CoCuMgNiZn)-oxide and (CoCrFeMnNi)-oxide are given in Figure 6.1. The respective trends have been colour coded as well as marked by arrows. For reproducibility of results, three data sets were recorded from each of the oxides and the best one plotted, which has less than 1% difference in values from the rest. It is evident from Figure 6.1 that sintered and quenched (CaCoFeMgNi)-oxide performs the least well, followed by (CoFeMgMnNi)-oxide. So far as (CoCuMgNiZn)-oxide is concerned, it yields the

maximum current density per incremental increase in voltage, however, (CoCrFeMnNi)-oxide outperforms the rest in terms of earliest onset to oxygen evolution reaction (OER). It may be discerned from the x-axis offsets from which the curves start rising with positive slopes (Figure 6.1). It is a common practice to provide some sort of activation to the specimen ink coated electrode, before recording the LSV response. This is usually done to coat the working electrode with oxide and hydroxide products on the surface, which is responsible for enhanced electrocatalytic activities. Surface oxygenation of active metal sites is believed to be key for evaluating catalytic response. Even if the specimen ink is not activated before the LSV response is recorded, analytical equations may be fitted from open circuit potential values or by IR (product of current and resistance) correction method post experiment. Subtraction of the solvent resistance effect and non-activation effect from the obtained plots is often done. These refinements in essence makes the LSV curves rise very steeply and sharply from the onset of OER overpotential. However, in the set of experiments discussed throughout this chapter, neither prior activation was provided nor post-mortem IR correction has been employed. Figure 6.1 depicts the raw response of the MCOs/HEOs and an attempt has been made to understand their trends from subsequent characterization of phase, microstructure and chemical distribution. They will be discussed in the subsequent sections. Figure 6.1 inset compares the LSV responses from equimolar quinary (CoCuMgNiZn)-oxide and its derivative equimolar ternary (CoMgNI)-oxide, in both sintered and quenched condition as well as sintered, quenched and aged condition. Both the current density response as well as overpotential response is better for higher-order oxide than its derivative lower order oxide.

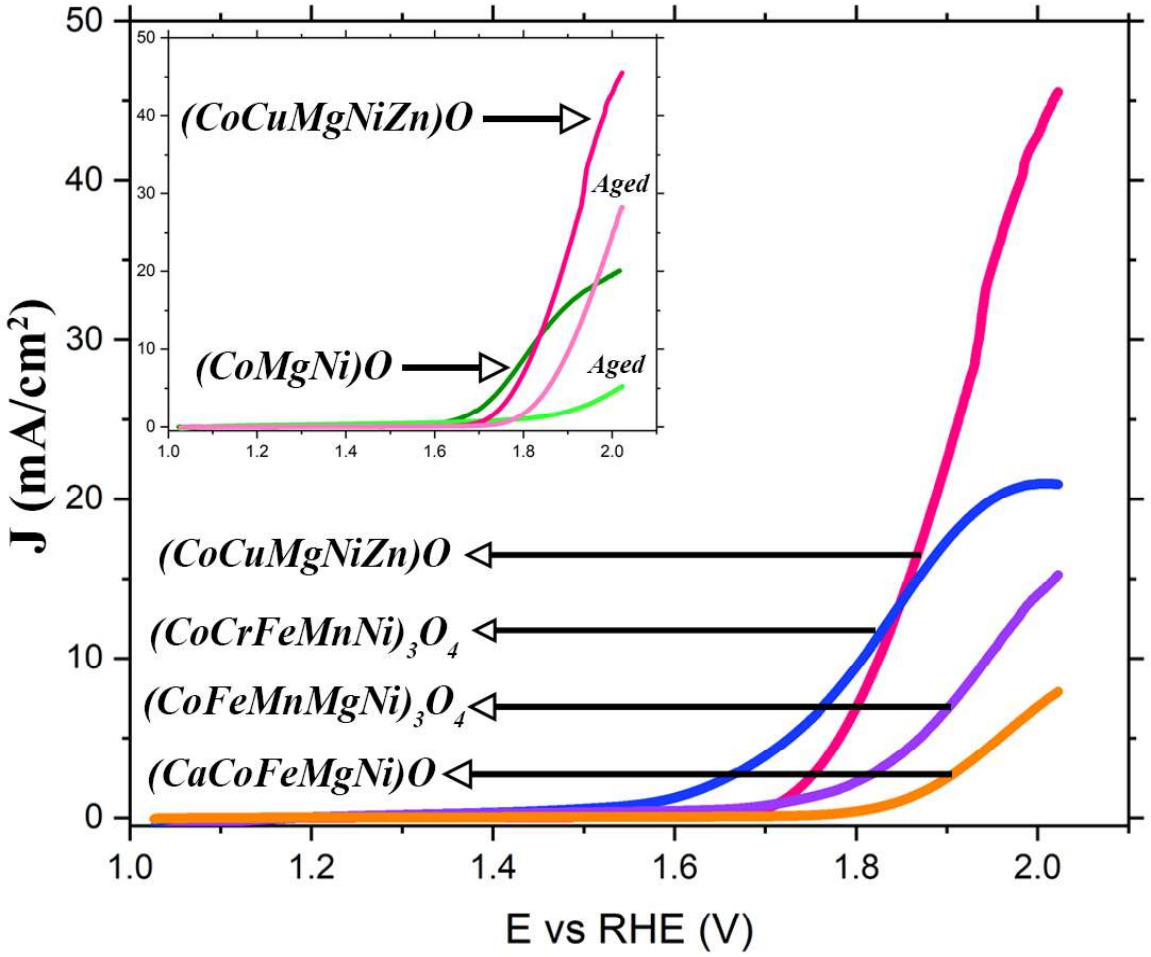

Figure 6.1: LSV plots recording the current density as a function of applied voltage, calibrated against reduced hydrogen electrode. The response from each oxide is colour coded. The inset compares the electrocatalytic response from (CoCuMgNiZn)-oxide and its derivative (CoMgNi)-oxide after sintering and ageing heat treatments.

Moreover, in both the ternary and quinary oxides, it is evident that with ageing heat treatment of the same compositions, a consistent deterioration of the electrocatalytic activity may be discerned (Marked in inset). The reasons for such performances and trends have been investigated through the systematic characterization and will be discussed subsequently.

Phase evolution of the respective MCOs and HEOs after solid-state synthesis, sintering and quenching are represented in the XRD patterns of Figure 6.2. It is observed that equimolar ternary (CoMgNi)-oxide crystallizes in a phase-pure rocksalt structure (a~4.22Å). The

major FCC peaks 111, 200, 220, 311 and 222 have been marked with filled circles. The ratio of the total integrated intensity of the 111 and 200 peaks also matched with simulated results. However, presence of very small volume fraction of a spinel phase (a~8.1Å) has been previously reported in this composition [16]. Partial substitution of Mn-ions in the ternary oxide yielded equimolar quaternary (CoMgMnNi)-oxide. Quaternary equimolar (CoMgMnNi)-oxide formed a mixture of two phases namely, rocksalt phase (a~4.22Å) and spinel phase (a~8.4Å) of roughly ~39% and 61% phase fraction respectively.

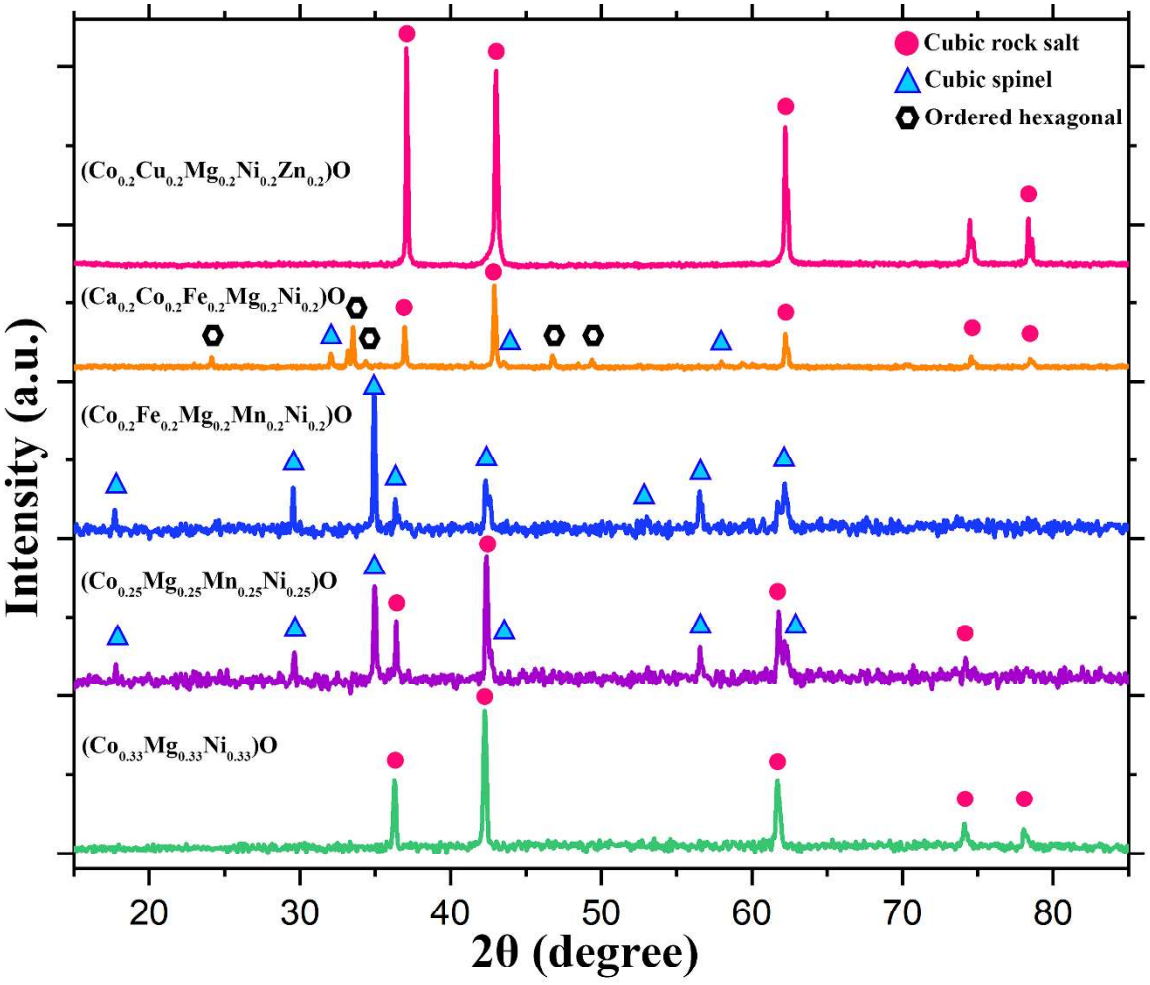

Figure 6.2. Experimental XRD patterns from sintered and quenched equimolar, ternary (CoMgNi)-oxide (green), quaternary (CoMgMnNi0-oxide (purple), quinary (CoFeMgMnNi)-oxide (blue), (CaCoFeMgNi)-oxide (orange) and (CoCuMgNiZn)-oxide (magenta). Respective phases have been marked with different coloured symbols.

Higher 2θ peaks of the rocksalt phase are absent, and shouldering of 200 and 220 peaks may be discerned, which may be indexed to 400 and 440 peaks of the spinel phase. Systematic addition of Fe-ions to the quaternary equimolar mixture of (CoMgMnNi)-oxide produced equimolar quinary (CoFeMgMnNi) HEO. It forms a single-phase spinel structure (a~8.38Å) globally, although systematic peak splitting and shouldering is observed. The XRD signature from sintered and quenched equimolar (CoCrFeMnNi) HEO also produced very similar pattern to that of (CoFeMgMnNi) HEO, as reported previously, and therefore it has not been shown in Figure 6.2 for the purpose of clarity [16]. Replacement of Mn-ions with Ca-ions in equimolar proportion produced quinary (CoFeMgMnNi)-oxide. It showed a complex diffraction pattern with several peaks. The major rocksalt phase (a~4.15Å) could easily be discerned, however, simulation methods had to be employed to retrieve the minor phases accurately, which has been reported elsewhere [17]. It has been found out that apart from a disordered rocksalt major phase, significant phase fraction of an ordered hexagonal phase (a~2.94Å, c~5.28Å) exists along with minor phase fraction of another rocksalt phase (a~4.78Å) and spinel phase (a~8.35Å) respectively. The approximate phase fractions were computed to be ~48%, ~35%, ~11% and 5% respectively. Finally, equimolar quinary (CoCuMgNiZn)-entropy stabilized oxide (ESO) crystallizes in a phase-pure rocksalt structure (a~4.23Å) on a global average. In its diffraction pattern, significant non-ideal intensity distribution between the 111 and 200 peaks may be discerned, along with systematic shouldering. It is envisaged that local composition modulation or Jahn-Teller induced local structural modulation or both may substantiate the experimental deviations from ideal structure, as has been reported earlier [18].

In order to rationalize the LSV behaviours of the four quinary MCOs/HEOs from Figure 6.1, microstructural characterization of the sintered and quenched pellets of the respective oxides have been carried out (Figure 6.3) by SEM and TEM techniques. Representative

SEM-SE images at two different magnifications, TEM BF/DF image and corresponding electron diffraction patterns have been shown for each of the four compositions in Figure 6.3. The common characteristic from all the SEM images is the uniform sintering of the pellets, which is estimated to be very close to its theoretical density, with minimal porosity observed. The sintered and quenched (CaCoFeMgNi)-oxide shows grainy morphology of varying size distribution and contrast (Figure 6.3-a1). The average grain size lies in the range of ~5-10 μm. Grains of dark contrast phase are occasionally engulfed by lighter contrast agglomerate phase (figure 6.3-a1(inset)). It has been confirmed earlier that the dark contrast phase is preferentially enriched in Co-, Ni- and Mg-ions while light contrast phase is enriched in Ca- and Fe-ions preferentially [17]. While the major rocksalt phase is found in (Co,Mg,Ni)-enriched areas, the minor phases of an ordered hexagonal structure, cubic rocksalt structure and cubic spinel structure are often found to coexist together in the (Ca,Fe)-enriched regions. They are found to share definite orientation relationship with one another, while sharing coherent/semi-coherent interphase interfaces among each other. A selected area electron diffraction pattern corroborating the same is given in Figure 6.3-a2. The three phases are marked in different colours, with their zone axis and principal vectors marked. Figure 6.3-a3 is dark field (DF) image from the ordered hexagonal phase, which is often found to exist independently from the other minor phases. Bands of alternating contrast may easily be discerned in the DF image, which are compound type of twins. The electron diffraction pattern clearly brings out systematic splitting of higher order spots, maintaining an angle of ~5.2 degrees (Figure 6.3-a3(inset)). The SEM-SE image from sintered and quenched (CoFeMgMnNi)-oxide in Figure 6.3-b1 shows bimodal grain size distribution with larger grains (~25 μm) surrounded by agglomerates of much finer grains (~3 μm). Porosity is also observed in between the grain size distribution.

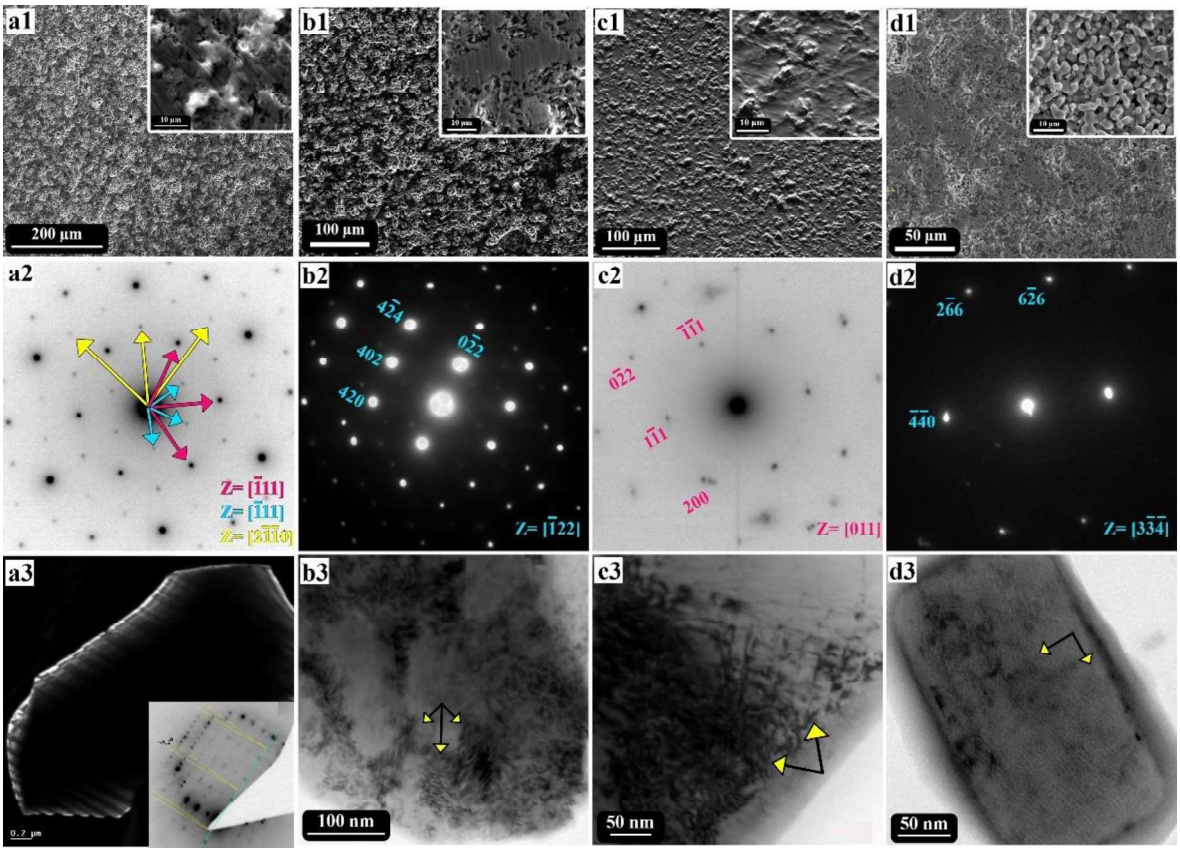

Figure 6.3: SEM-SE micrographs, selected area diffraction pattern and TEM bright field/dark field images from sintered and quenched (a1-a3) (CaCoFeMgNi)-oxide, (b1-b3) (CoFeMgMnNi)-oxide, (c1-c3) (CoCuMgNiZn) ESO and (d1-d3) (CoCrFeMnNi) HEO respectively. The microstructural features are marked with arrows and indexing of diffraction patterns have been done employing different colour schemes.

Fine sub-micron bands of dark contrast may be discerned within the larger grains (Figure 6.3-b1(inset)). The selected area diffraction pattern may be indexed to a z=[1̄22] zone axis of a cubic spinel phase (Figure 6.3-b2). However, clear modulation of intensity and bulging of the first order spots may be discerned. The corresponding bright field image shows mottled contrast in the single crystal grain body, with occasional fringe contrast, which are marked by arrows (Figure 6.3-b3). The SEM image in Figure 6.3-c1 of (CoCuMgNiZn) ESO shows uniform grain size distribution with finer agglomerates. The sub-grain structure is visible within the agglomerate clusters, with minimal porosity (Figure 6.3-c1(inset)). Selected area diffraction pattern from z=[011] zone axis confirms a global average single-

phase rocksalt structure, however with shape evolution and splitting of spots (Figure 6.3-c2). The corresponding BF image in Figure 6.3-c3 shows fringe contrast along with domain structure (marked with arrows). The SEM image from a region of interest in sintered and quenched (CoCrFeMnNi) HEO again shows uniform sintering with bimodal grain size distribution (Figure 6.3-d1). The finer colonies have roughly spherical shaped particles of ~2μm, interconnected with one another (Figure 6.3-d1(inset)). A representative electron diffraction pattern from the average single-phase with spinel structure is depicted in Figure 6.3-d2. It conforms to the z=[33$\bar{4}$] zone axis single crystal pattern, however, bulging and onset of splitting of the 440 type of spots may be seen. The corresponding bright field image in Figure 6.3-d3 shows fine nano-domain contrast, which are arranged mutually perpendicular to each other (marked with arrows). It has been previously shown that they are interweaved fringes, with in between domain size of ~5-10 nm [16]. It may be concluded from the above observations combined, that local structural modulation within a global average single-phase in quinary ESO/HEO enhances the electrocatalytic performance in contrast to phase-pure ternary or multi-phase quinary oxides.

In order to rationalize the drop in electrocatalytic activity with ageing, SEM-XEDS maps have been collected from both equimolar ternary (CoMgNi)-oxide as well as (CoCuMgNiZn) ESO (Figure 6.4(a-b)). Elemental mapping has been carried out on pellets of the same composition (a1,a2 and b1,b2), one after sintering at 1323K for 10h followed by water quenching (a1,b1) and the other one after sintering followed by ageing at 723K for 100h (a2,b2).

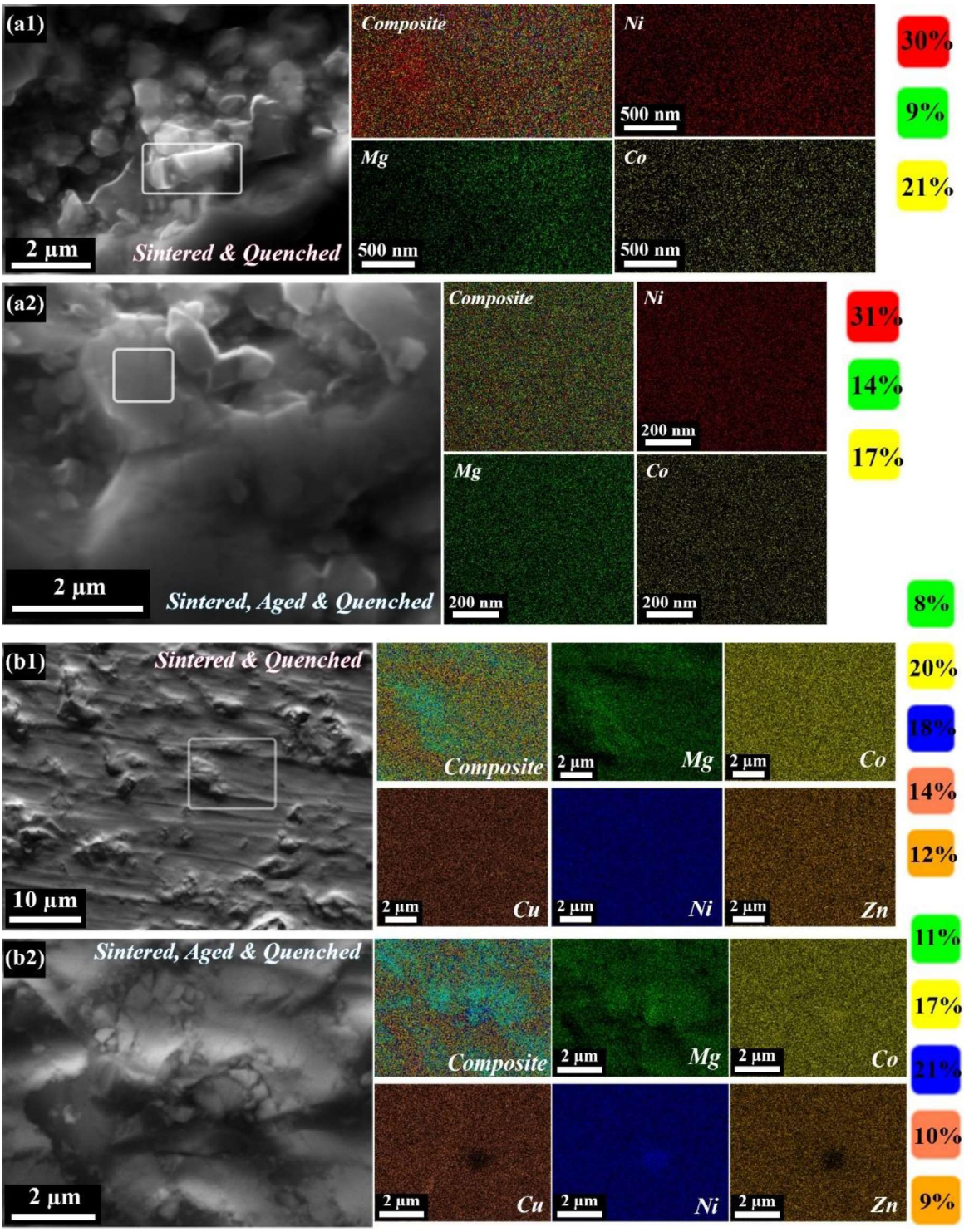

Figue 6.4: SEM-XEDS chemical mapping from (a1) sintered and quenched (CoMgNi)-oxide, (a2) sintered, aged and quenched (CoMgNi)-oxide, (b1) sintered and quenched (CoCuMgNiZn) ESO and (b2) sintered, aged and quenched (CoCuMgNiZn) ESO respectively. The quantification of the cation weight % has been provided in coloured boxes adjacent to the respective maps.

It may be easily discerned from the chemical quantification of the respective cation K-shell excitations in both the oxides, that the surface composition gets altered after ageing heat treatment. The ternary (CoMgNi)-oxide shows a significant enrichment of Mg-ions after ageing, however with a depletion of Co-ions and similar concentration of Ni-ions (Figure 6.4a1-a2). Similarly, in (CoCuMgNiZn) ESO after ageing, a significant depletion of Co-, Cu- and Zn-ions may easily be discerned, with enrichment in Mg- and Ni-ions (Figure 6.4b1-b2). Preferential micro-segregation of ionic species may be seen in SEM-XEDS composite maps. Since surface composition, especially the concentration of redox active cation sites determines the electrocatalytic activity, the drop in performance after ageing heat treatment becomes clear from the chemical distribution maps.

The current density (J) has been plotted against the reduced hydrogen potential (RHE) for equimolar quaternary (CoMgMnNi)-oxide in Figure 6.5a. For reproducibility of results, three linear sweep voltammetry (LSV) curves have been plotted. It shows the best electrocatalytic activity among all the other HEO/ESO or multicomponent oxides reported in this chapter. Equimolar quaternary (CoMgMnNi)-oxide records the steepest slope among the rest, which points to the enhanced conductivity of the multicomponent oxide. It has also recorded the highest current density along with the lowest overpotential to achieve 10 mA/cm^2. The cyclic voltammetry (CV) test was carried out on the same composition at different scan rates and is plotted in Figure 6.5b. It is seen that with progressively higher scan rates, the area under the hysteresis loop keeps on increasing. This points to the enhanced efficiency of redox reaction rates. However, no significant oxidation and reduction peaks could be discerned in the CV curves. It is recalled that equimolar quaternary (CoMgMnNi)-oxide shows a two-phase mixture of spinel and rocksalt phases (Figure 6.2 in purple).

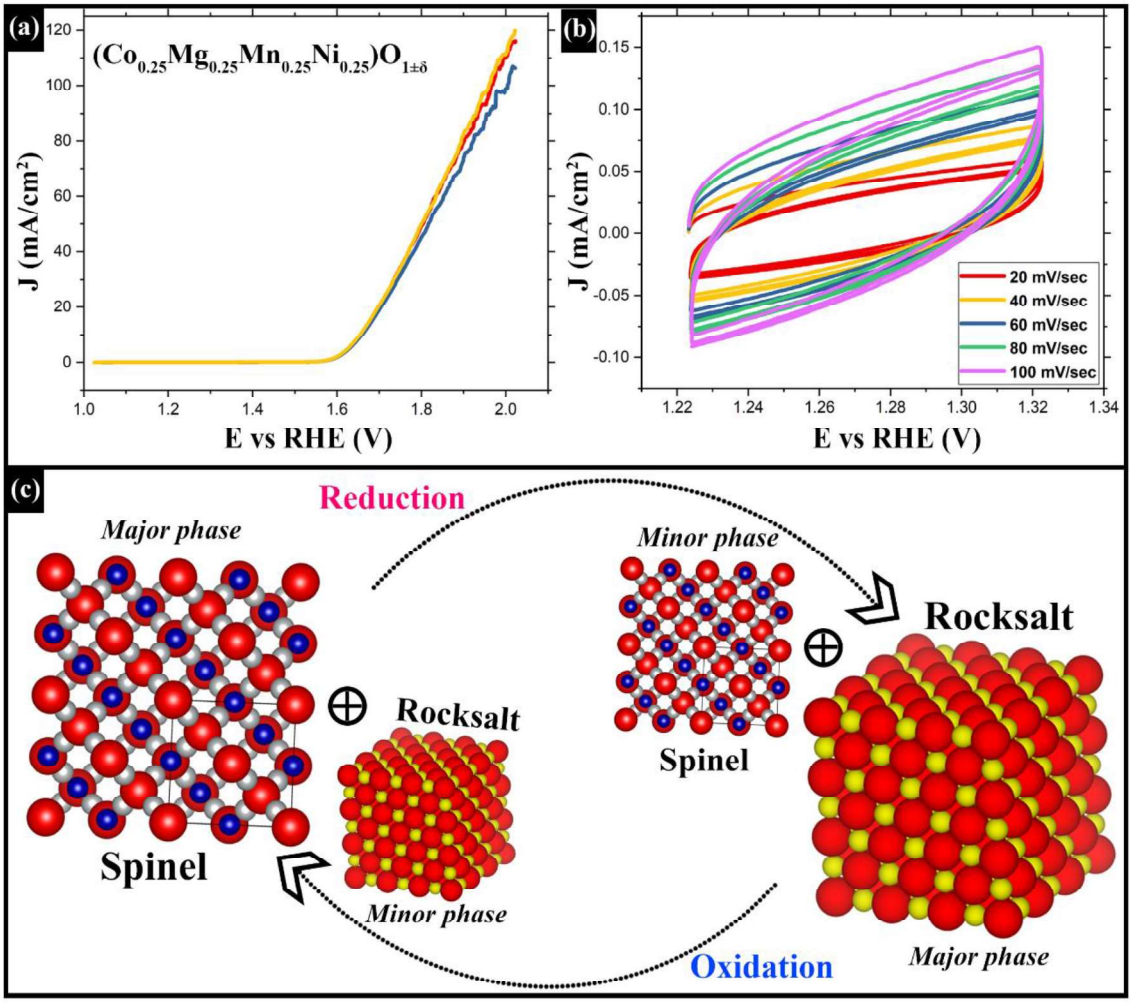

Figure 6.5: (a) LSV response from sintered and quenched equimolar (CoMgMnNi)-oxide, (b) CV plots from the same oxide under varying scan rates and (c) schematic representing possible mechanism behind enhanced electrocatalytic activity in the dual-phase oxide.

It is also previously reported that dual-phase (CoFeMgMn)-oxide drastically lowers the temperature of a two-step thermochemical water-splitting via interconversion of rocksalt and spinel phases during heating and cooling [19]. In order to rationalize the superior performance of sintered and quenched (CoMgMnNi)-oxide based on the current observations and the school of thought proposed earlier, a schematic representation has been depicted in Figure 6.5c. The possible interconversion between spinel and rocksalt phases in varying phase fractions during oxidation and reduction cycles is thought to enhance the electrocatalytic activity in this multicomponent oxide [19]. In this process, the

thermodynamic cycle becomes essentially a redox heat engine due to the continuous exchange of oxygen. The lattice oxygen mechanism (LOM) is more likely to be operational.

The overpotential plots and the Tafel slopes of all the oxides have been plotted in Figure 6.6a-b. Figure 6.6a represents the bar diagram of the overpotential required to cross current density of 5 mA/cm^2 for the respective oxides. The overpotential values at 1 mA/cm^2 and at 10 mA/cm^2 is reported in white and black respectively. The equimolar quaternary (CoMgMnN)-oxide shows the least overpotential values at all possible current densities, followed by singl-phase spinel structured (CoCrFeMnNi) HEO followed by phase-pure rocksalt structured (CoCuMgNiZn) ESO. It is also to be noted that the spread in the recorded overpotential values to achieve 1, 5 and 10 mA/cm^2 current density respectively, is quite high for most of the oxides barring quaternary (CoMgMnNi)-oxide. This further validates the solvent resistance and non-activation effect of the specimen inks. Multi-phase (CaCoFeMgNi)-oxide and single-phase (CoMgNi)-oxide shows the highest overpotential values and performs the poorest. Correspondingly, the Tafel slope is the lowest for (CoMgMnNi)-oxide while it is the highest for (CaCoFeMgNi)-oxide (Figure 6.6b).

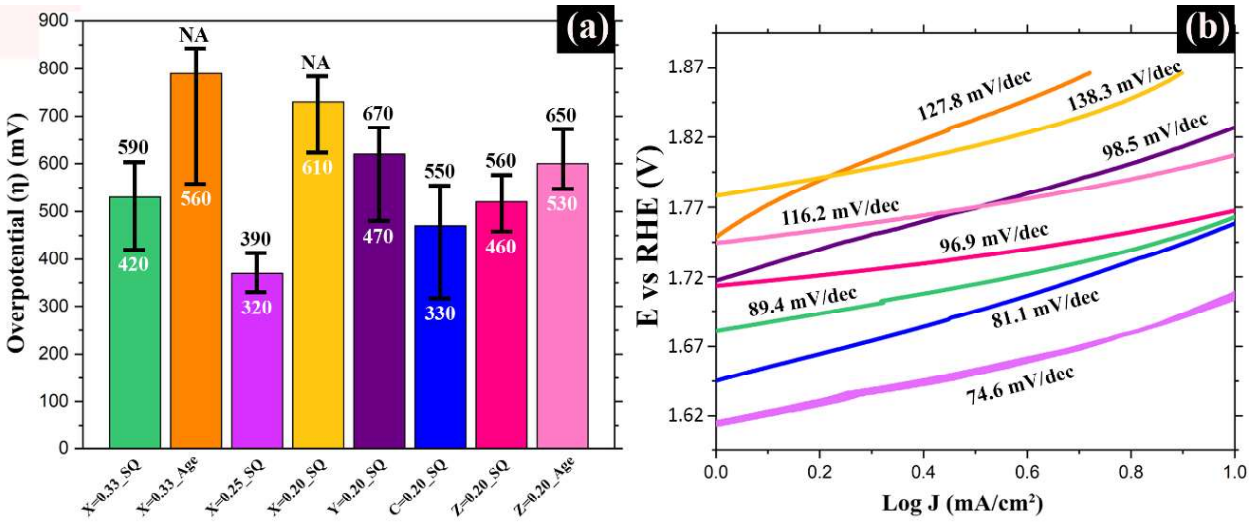

Figure 6.6: (a) Overpotential plots for all the respective multicomponent oxides at 5 mA/cm^2 and (b) Tafel slopes for the same oxides. The histogram is accompanied with computed overpotential values at 1 mA/cm^2 (in white) and at 10 mA/cm^2 (in black). The Tafel slopes are marked over each oxide.

6.4. Conclusions

It may be concluded from the present study that equimolar quaternary (CoMgMnNi)-oxide is a potential candidate for efficient electrocatalysis, recording a low overpotential of 390 mV to achieve a current density of 10 mA/cm^2 with a Tafel slope of ~74.6 mV/dec. It is thought that the possible interconversion between spinel and rocksalt phases in varying phase fractions during oxidation and reduction cycles enhances the redox activity of the material. It thus becomes likely that the lattice oxygen mechanism (LOM) becomes operative over and above adsorbate evolution mechanism (AEM) during the interconversion between spinel and rocksalt phases. Equimolar quinary (CaCoFeMgNi)-oxide performs the poorest as electrocatalyst, owing to large scale chemical segregation and multi-phase nature. Both the (CoCrFeMnNi) HEO characterized by spinel structure and (CoCuMgNiZn) ESO characterized by rocksalt structure show encouraging electrocatalytic performance, which scope for further enhancement. This is attributed to the local structural modulation in both the compositions, with or without associated fine-scale compositional modulation. Moreover, lower order derivative oxides perform poorer compared to similar structured higher order oxide. Furthermore, probable change in bulk chemistry and a definite change in surface chemistry in the multicomponent oxides occurs during ageing treatment, which in turn affects the electrocatalytic activity for the worse. While Co-, Ni-, Fe-, Mn-ions are known to enhance the conductivity of the catalysts, enrichment of Mg-ions is known to stabilize a particular kind of phase and hence reduce the catalytic response.

6.5. Reference

1. C. Liu, F. Li, L. P. Ma, H. M. Cheng, Advanced materials for energy storage, Adv. Mater., 2010, 22, E28-E62
2. B. C. H. Steele, A. Heinzel, Materials for fuel-cell technologies, Nature, 2001, Vol. 414, 345-352
3. X. Yu, Z. Tang, D. Sun, L. Ouyang, M. Zhu, Recent advances and remaining challenges of nanostructured materials for hydrogen storage applications, Prog. Mater. Sci., 2017, Vol. 88, 1-48
4. A. S. R. Bati, M. Batmunkh, J. G. Shapter, Emerging 2D layered materials for perovskite solar cells, Adv. Energy Mater., 2019, 1902253 (21 pages)
5. J. Knaster, A. Moeslang, T. Muroga, Materials research for fusion, Nature Physics, 2016, Vol. 12, 424-434
6. J. Baek, M. D. Hossain, P. Mukherjee, J. Lee, K. T. Winther, J. Leem, Y. Jiang, W. C. Chueh, M. Bajdich, X. Zheng, Synergistic effects of mixing and strain in high entropy spinel oxides for oxygen evolution reaction, Nat. Commun., 2023, Vol. 14 (5936), 1-11
7. L. Sharma, N. K. Katiyar, A. Parui, R. Das, R. Kumar, C. S. Tiwary, A. K. Singh, A. Halder, K. Biswas, Low-cost high entropy alloy (HEA) for high-efficiency oxygen evolution reaction (OER), Nano Research, 2022, Vol. 15 (6), 4799-4806
8. D. Wang, C. Duan, Y. Yu, X. Li, Z. Wang, Y. Liu, C. Liu, Co-regulation of anion-cation in transition metal high entropy oxide for outstanding OER electrocatalytic performance, Journal of Alloys and Compounds, 2023, Vol. 967, 171758
9. Y. Liu, X. Zhang, Metamaterials: a new frontier of science and technology, Chem. Soc. Rev., 2011, Vol. 40, 2494-2507
10. N. I. Zheludev, Y. S. Kivshar, From metamaterials to metadevices, Nature Materials, 2012, Vol. 2, 917-924

11. J. B. Goodenough, Perspective on engineering transition-metal oxides, Chemistry of Materials, 2014, Vol. 26, 820-829
12. M. Anandkumar, E. Trofimov, Synthesis, properties, and applications of high-entropy oxide ceramics: Current progress and future perspectives, Journal of Alloys and Compounds, 2023, Vol. 960, 170690
13. D. Berardan, S. Franger, D. Dragoe, A. K. Meena, N. Dragoe, Colossal dielectric constant in high entropy oxides, Phys. Status Solidi RRL, 2016, Vol. 10 (4), 328-333
14. D. Berardan, S. Franger, A. K. Meena, N. Dragoe, Room temperature lithium superionic conductivity in high entropy oxides, J. Mater. Chem. A, 2016, Vol. 4, 9536
15. Z. Y. Liu, Y. Liu, Y. Xu, H. Zhang, Z. Shao, Z. Wang, H. Chen, Novel high-entropy oxides for energy storage and conversion: From fundamentals to practical applications, Green Energy and Environment, 2023, Vol. 8, 1341-1357
16. S. Mukherjee, N. K. Mukhopadhyay, J. Basu, Structural modulation and oriented growth of rocksalt and spinel phases in equimolar multicomponent {Co(Cr/Mg)FeMnNi}-oxide and its derivatives, J. Am. Ceram. Soc., 2025, e20619 (15 pages)
17. S. Mukherjee, N.K. Mukhopadhyay, J. Basu, Composition modulation, strain minimization and oriented growth of phases in equimolar (CaCoFeMgNi) multicomponent oxide, Acta Mater., 2025, 285, 120621 (12 pages)
18. S. Mukherjee, N.K. Mukhopadhyay, J. Basu, Local composition modulation and oriented inter-growth induced strain minimization in entropy stabilized (CoCuMgNiZn) oxide [Communicated]
19. S. Zhai, J. Rojas, N. Ahlborg, K. Lim, M. F. Toney, H. Jin, W. C. Chueh, A. Majumdar, The use of ply-cationic oxide to lower the temperature of two-step thermochemical water-splitting, Energy & Environmental Science, 2018, Vol. 11, 2172-2178